JOURNAL OF GEOPHYSICAL RESEARCH: PLANETS, VOL. 118, 2520–2536, doi:10.1002/2013JE004513, 2013

Material ejection by the cold jets and temperature evolution of the south seasonal polar cap of Mars from THEMIS/CRISM observations and implications for surface properties

C. Pilorget,[1] C. S. Edwards,[1] B. L. Ehlmann,[1,2] F. Forget,[3] and E. Millour[3]

Received 30 August 2013; revised 8 November 2013; accepted 11 November 2013; published 23 December 2013.

[1] As the seasonal CO_2 ice polar caps of Mars retreat during spring, dark spots appear on the ice in some specific regions. These features are thought to result from basal sublimation of the transparent CO_2 ice followed by ejection of regolith-type material, which then covers the ice. We have used Compact Reconnaissance Imaging Spectrometer for Mars (CRISM) reflectance data, Thermal Emission Imaging System (THEMIS) visible images, and THEMIS-derived temperature retrievals along with a thermal numerical model to constrain the physical and compositional characteristics of the seasonal cap for several areas exhibiting dark spots at both high spatial and temporal resolutions. Data analysis suggests an active period of material ejection (before solar longitude (Ls) 200), accumulation around the ejection points, and spreading of part of the ejected material over the whole area, followed by a period where no significant amount of material is ejected, followed by complete defrosting ($\approx$ Ls 245). Dark material thickness on top of the CO_2 ice is estimated to range from a few hundreds of microns to a few millimeters in the warmest spots, based on numerical modeling combined with the observed temperature evolution. The nature of the venting process and the amount of material that is moved lead to the conclusion that it could have an important impact on the surface physical properties.

Citation: Pilorget, C., C. S. Edwards, B. L. Ehlmann, F. Forget, and E. Millour (2013), Material ejection by the cold jets and temperature evolution of the south seasonal polar cap of Mars from THEMIS/CRISM observations and implications for surface properties, *J. Geophys. Res. Planets*, *118*, 2520–2536, doi:10.1002/2013JE004513.

1. Introduction

[2] On Mars, about one third of the atmosphere (composed of 95% CO_2) condenses during fall and winter to form polar caps [*James et al.*, 1992]. Because of pressure and temperature conditions at the surface, there is no CO_2 liquid phase and solid CO_2 directly condenses and sublimates. During spring, the insolation increases and the seasonal polar cap disappears gradually (except in the southern very high latitudes where a small perennial polar cap remains).

[3] This recession has been monitored extensively by visible, near-infrared, and thermal-infrared instruments [*Kieffer et al.*, 2000; *Titus et al.*, 2001; *Langevin et al.*, 2007; *Appéré et al.*, 2011]. At large spatial scale, the evolution of the south seasonal cap is highly asymetric: During spring a fraction of the south seasonal cap exhibits a "cryptic" behavior characterized by a temperature close to the CO_2 condensation point ($T_{cond}^{surf} \approx 145$ K at the Martian surface pressure), a low albedo (darker than CO_2 ice, close to that of defrosted surfaces), and a weak CO_2 ice spectral signature [*Kieffer et al.*, 2000; *Langevin et al.*, 2006, 2007]. CO_2 ice remains within the region exhibiting a "cryptic" behavior until $\approx$ Ls 270, whereas it remains longer in surrounding areas until $\approx$ Ls 300 [*Kieffer et al.*, 2000; *Langevin et al.*, 2007].

[4] The Mars Global Surveyor (MGS) Mars Orbiter Camera and Mars Reconnaissance Orbiter High Resolution Imaging Science Experiment (HiRISE) have returned high-resolution images of these polar regions unveiling numerous exotic features. Dark spots and fans appear on the surface during the seasonal polar cap recession, thus leading to the low albedo regions that were previously observed at larger scale. Many of these features look like exposures of subfrost soil and have been interpreted as such [*Malin and Edgett*, 2000; *Supulver et al.*, 2001], but the Thermal Emission Imaging System (THEMIS) observations showed that they remain near the temperatures expected for solid CO_2 and therefore must be composed (at least partially) of dark material in intimate contact with CO_2 ice [*Kieffer et al.*, 2006]. Thermal Emission Spectrometer (TES) observations over the cryptic region have also highlighted unexpected high temperatures and diurnal variations of a few Kelvins [*Kieffer et al.*, 2000].

Additional supporting information may be found in the online version of this article.

[1]Division of Geological and Planetary Sciences, Caltech, Pasadena, California, USA.
[2]Jet Propulsion Laboratory, Caltech, Pasadena, California, USA.
[3]Laboratoire de Météorologie Dynamique, CNRS/UPMC/IPSL, Paris Cedex 05, France.

Corresponding author: C. Pilorget, Division of Geological and Planetary Sciences, Caltech, Pasadena, CA 91125, USA. (cpilorge@caltech.edu)

©2013. American Geophysical Union. All Rights Reserved.
2169-9097/13/10.1002/2013JE004513

[5] A proposed explanation for dark spots in the cryptic region is that CO_2 ice is in the form of slab ice with large photon path lengths (typically a few tens of centimeter) [*Kieffer*, 2007]. During spring, solar radiation penetrates into the CO_2 slab and heats the regolith, thus leading to basal sublimation. Gas forms, and when a path to the surface is created, CO_2 gas and some material from the underlying regolith are ejected and form these dark spots [*Piqueux et al.*, 2003; *Kieffer*, 2007; *Portyankina et al.*, 2010]. *Pilorget et al.* [2011] have modeled this process and demonstrated that basal sublimation is indeed expected to occur on Mars in the case of a clean large-grained CO_2 ice (grain size typically greater than a few centimeter and dust content less than a few tens of parts per million). Other surveys using HiRISE and CRISM observations have also supported this explanation [*Titus et al.*, 2007; *Hansen et al.*, 2010a; *Thomas et al.*, 2010; *Pommerol et al.*, 2011]. This process is proposed to be a major erosive agent in the polar regions and thus could significantly affect the preservation of the near-surface stratigraphic record [*Piqueux and Christensen*, 2008; *Hansen et al.*, 2010a].

[6] In this paper, we present a coupled THEMIS/CRISM data analysis of several areas exhibiting a cryptic behavior in the south seasonal cap, with a special emphasis on the dark material cover on top of the CO_2 ice. These data are then compared to the results of a numerical model simulating the thermal behavior of the "cryptic" areas. Our main objectives are as follows:

[7] 1. To study the temporal and spatial evolution of the dark material layer covering the CO_2 ice, combining albedo, temperature, and CO_2 ice absorption band depth at high spatial resolution.

[8] 2. To constrain the thickness of the dark material layer using numerical modeling.

[9] 3. To link this venting process to the surface properties observed at high latitudes.

2. Methodology

2.1. Introduction

[10] The CO_2 sublimation/condensation temperature directly depends on the surface pressure. It can be estimated in our temperature range by using *James et al.* [1992]

$$\ln(p) = 26.1228 - \frac{3385.26}{T} - 9.4461 \times 10^{-3}\, T \qquad (1)$$

with p the surface pressure and T the condensation temperature, thus leading to a temperature of 144.8 K for a mean surface pressure of 400 Pa, as estimated in the southern polar regions. This temperature is referred to as $T_{\mathrm{cond}}^{\mathrm{surf}}$ in what follows.

[11] The presence of a thin layer of opaque material on top of CO_2 ice leads to an increase of the surface temperature: The dark grains absorb the solar flux and warm up. The presence of CO_2 ice underneath nevertheless limits this temperature increase since the CO_2 ice remains at $\approx T_{\mathrm{cond}}^{\mathrm{surf}}$ (see section 4.2).

[12] THEMIS IR data are used to retrieve the surface temperature during spring in different regions of the south seasonal polar cap of Mars that exhibit dark spots (see section 2.2). The THEMIS IR data have a spatial sampling of 100 m, so temperatures are potentially a spatial mixture of dark material-covered areas (with $T_{\mathrm{surf}} > T_{\mathrm{cond}}^{\mathrm{surf}}$) and non-dark material-covered areas (with $T_{\mathrm{surf}} = T_{\mathrm{cond}}^{\mathrm{surf}}$). THEMIS data are therefore coupled to CRISM data (which have a spatial sampling of $\approx$ 18 m) to better constrain these potential mixtures. Together, these data are used to determine the evolution of the surface properties during spring and are then compared to results from a numerical model in particular to constrain the thickness of the dark material layer.

2.2. Regions of Interest

[13] The south polar region has been extensively observed during spring by the CRISM and THEMIS instruments for several years. We have selected here five regions of interest (ROIs) because of the large number of observations and high temporal resolution from both THEMIS and CRISM instruments during spring of Martian year 28 (MY28):

[14] 1. Manhattan Island (–86N, 100E)

[15] 2. Ithica (–85N, 179E)

[16] 3. Starfish (–84N, 241E)

[17] 4. Inca City (–81N, 295E)

[18] 5. Dolomedes (–87N, 174E)

[19] From these five ROIs, which all exhibit a cryptic behavior, three are actually located inside the main "cryptic" region as defined by *Kieffer et al.* [2000] (Manhattan Island, Dolomedes, and Ithica) and two are located outside (Inca City and Starfish). A coupled HiRISE/CRISM survey has also been performed over these regions, allowing direct comparison with our results [*Pommerol et al.*, 2011]. While images were not acquired on the same day, THEMIS and CRISM data can be correlated over similar Ls ranges.

2.3. THEMIS Data Set

[20] THEMIS is a multispectral imager on board Mars Odyssey that operates in the thermal infrared (between 6.5 and 15 μm, with a spatial sampling of 100 m) and in the visible/near-infrared (between 450 and 850 nm, with a spatial sampling of 18, 36, or 72 m) spectral ranges [*Christensen et al.*, 2004]. The observed Martian radiance measured by THEMIS in the thermal infrared at nadir can be approximated to first order as follows:

$$I_{\mathrm{obs}}(\lambda) = \epsilon(\lambda) B\,[\lambda, T_{\mathrm{surf}}]\, e^{-\tau_0(\lambda)} + \int_0^{\tau_0} B\,[\lambda, T(p)]\, e^{-\tau(\lambda,p)} \mathrm{d}\tau \qquad (2)$$

with $\epsilon(\lambda)$, the surface emissivity; $B\,[\lambda, T_{\mathrm{surf}}]$, the blackbody radiance as a function of the surface temperature T_{surf}; and $\tau(\lambda, p)$, the normal opacity profile as a function of wavelength and pressure. The integral is taken through the atmosphere from the spacecraft ($\tau = 0$) to the surface ($\tau = \tau_0$) and $T(p)$ is the atmospheric temperature profile. The first term accounts for the emission of surface radiation and its absorption by the atmosphere, whereas the second term accounts for the radiation emitted by the atmosphere and suspended aerosols.

[21] The region from 8 to 12 μm ($\approx$ 850 to 1200 cm^{-1}) is strongly influenced by atmospheric dust, whereas the region longward of 13 μm is affected by the 15 μm ($\approx$ 400 cm^{-1}) band of CO_2. The band 9 brightness temperature (12.17–12.98 μm, referred to as T_{THEMIS}^{12} in what follows) is the least affected by the atmosphere in this spectral range, while maintaining a high signal-to-noise ratio. The emissivity of the ejected regolith material is expected

to be close to 1 over this spectral range. CO_2 ice emissivity, however, may change with grain size and dust/water ice inclusions [*Warren et al.*, 1990; *Kieffer et al.*, 2000]. *Pilorget et al.* [2011] demonstrated that basal sublimation was only possible for CO_2 ice with large path lengths and low amount of impurities. Emissivity of this kind of CO_2 ice is also close to 1 at the wavelength chosen. Thus, assuming a surface emissivity of 1, T^{l2}_{THEMIS} is used as a proxy for the surface kinetic temperature.

[22] Atmospheric opacity is mostly driven by the presence of dust over this spectral range. The dust opacity is, however, not well constrained over the polar regions. Moreover, it is especially difficult to evaluate over the regions exhibiting a cryptic behavior as dust is also present on the surface as part of the material covering the CO_2 ice. *Kieffer et al.* [2000] as well as *Vincendon and Langevin* [2010] estimated the atmospheric dust opacity over the southern polar region during spring to range between 0.1 and 0.3 (values at 9 μm) with possible sporadic increases up to 0.4 due to dust clouds. More recently, (S. Douté, Monitoring atmospheric dust spring activity at high Q7 southern latitudes on Mars using OMEGA, submitted to *Icarus*, 2013) showed that the dust opacity over the the cryptic region remains between 0.3 and 0.4 at 1 μm, thus around 0.15–0.2 at 9 μm, prior to Ls 240. Using equation (2), we can estimate an order of magnitude of the influence of the dust on the measured temperature. *Smith et al.* [2000a, 2000b] results show that the dust opacity over THEMIS band 9 (12.17–12.98 μm) corresponds roughly to $0.3\tau_{9\mu\mathrm{m}}$. Assuming an atmospheric temperature of the atmosphere of 180 K and an homogeneous distribution of dust, we can estimate the bias on the retrieved temperature to be $\Delta T = +4$K for $\tau_{9\mu\mathrm{m}} = 0.2$ and $\Delta T = +7$K for $\tau_{9\mu\mathrm{m}} = 0.4$.

[23] The noise-equivalent delta temperature, i.e., precision, can be computed using *Christensen et al.* [2004] and is estimated to be $\approx$ 3 K at 148 K, thus allowing detection of small temperature contrasts within an image. THEMIS data that are used to retrieve the surface temperature were acquired typically between 7 A.M. and 5 P.M. (local time). The effect of diurnal variations is discussed in section 4.2.

[24] TES data are used to confirm surface temperature retrievals by THEMIS. TES is a spectrometer on board Mars Global Surveyor (MGS) working in the thermal infrared from 6 to 50 μm with a spatial sampling of $\approx$ 3 km [*Christensen et al.*, 2001]. No data were acquired in Martian year 28 ("MY28"), as the MGS spacecraft failed in early MY28. However, data from MY24, MY25, and MY26 (no data were available over these regions in MY27) are used to confirm the trends that were observed by THEMIS in MY28, assuming that the processes repeat quasi-similarly year after year [*Hansen et al.*, 2010b]. TES data used to retrieve the surface temperature were acquired between 9 A.M. and 9 P.M. (local time).

[25] The surface temperature is derived from TES maximum brightness temperature between 20 and 33 μm (referred to as T^{30}_{TES} in what follows), as the atmosphere is rather transparent in this spectral range. T_{TES} at 26 μm is strongly influenced by the CO_2 ice grain size and dust inclusions [*Kieffer et al.*, 2000], and thus, T^{30}_{TES} is also slightly influenced by these properties. However, as previously mentioned, for a large-grained and "clean" CO_2 ice, the emissivity is $\approx$ 1. *Smith et al.* [2000a, 2000b] results show that the dust opacity over that spectral range corresponds roughly to $0.35\tau_{9\mu\mathrm{m}}$. Assuming a temperature of the atmosphere of 180 K and an homogeneous distribution of dust, we can estimate the bias on the retrieved temperature to be $\Delta T = +3$K for $\tau_{9\mu\mathrm{m}} = 0.2$ and $\Delta T = +5$K for $\tau_{9\mu\mathrm{m}} = 0.4$. TES temperatures are therefore expected to be a little closer from the surface kinetic temperature than the THEMIS-based retrievals.

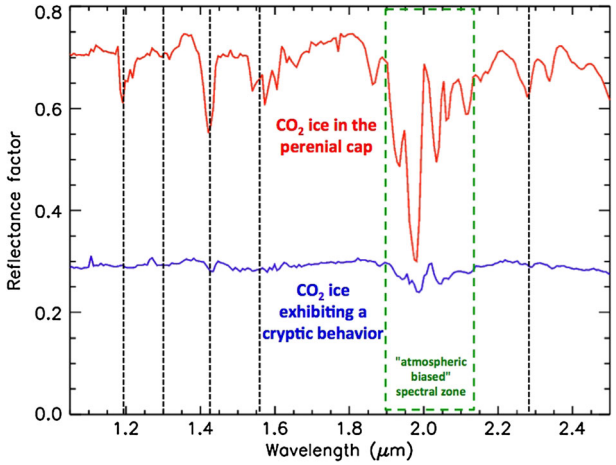

Figure 1. Examples of CRISM CO_2 ice spectra. Red line shows that one has been acquired over the perennial cap at Ls 233 (–87.0N, 328.2E) and exhibits typical CO_2 ice spectral features with a high reflectance and strong absorption features at 1.42 and 2.28 μm. Smaller features can also be observed at 1.2, 1.3, and 1.56 μm. Another strong feature occurs around 2 μm but overlaps with absorptions due to atmospheric CO_2. Blue line shows the one has been acquired over the Manhattan Island region (–87.0N, 101.0E, at a dark spot location) and exhibits a typical "cryptic" behavior with a low reflectance coupled with very weak CO_2 ice features.

[26] THEMIS 18 m/pixel visible images acquired simultaneously with thermal IR images are also used as an indicator of the dark spot activity.

2.4. CRISM Data Set

[27] CRISM is a hyperspectral imager in the visible and near-infrared (0.4–4.0 μm) on board the Mars Reconnaissance Orbiter [*Murchie et al.*, 2007]. Calibrated data of surface reflectance, corrected for the atmophere, are obtained using the CAT (CRISM Analysis Toolkit) software released by the CRISM team [*Morgan et al.*, 2009]. The spatial sampling varies with the observations from $\approx$18 to 40 m. In what follows, only FRT (full resolution target), which have a spatial sampling of $\approx$18–20 m, are used.

[28] CRISM spectra provide constraints on the composition of the regions studied. CO_2 ice can be identified in the near-infrared through several diagnostic spectral absorption features at 1.42 and 2.28 μm [*Langevin et al.*, 2007]. We use here the CO_2 ice criterion for CRISM data that measures the band depth at 1.42 μm [*Murchie et al.*, 2007]. Cryptic behavior (defined as dark material at $\approx T^{\mathrm{surf}}_{\mathrm{cond}}$) corresponds to a decrease in both the reflectance and strength of CO_2 ice absorption features [*Langevin et al.*, 2006, 2007], as shown in Figure 1. Water ice deposition on top of the CO_2 ice has also been detected in the southern polar regions [*Bibring et al.*, 2004; *Langevin et al.*, 2007; *Brown et al.*,

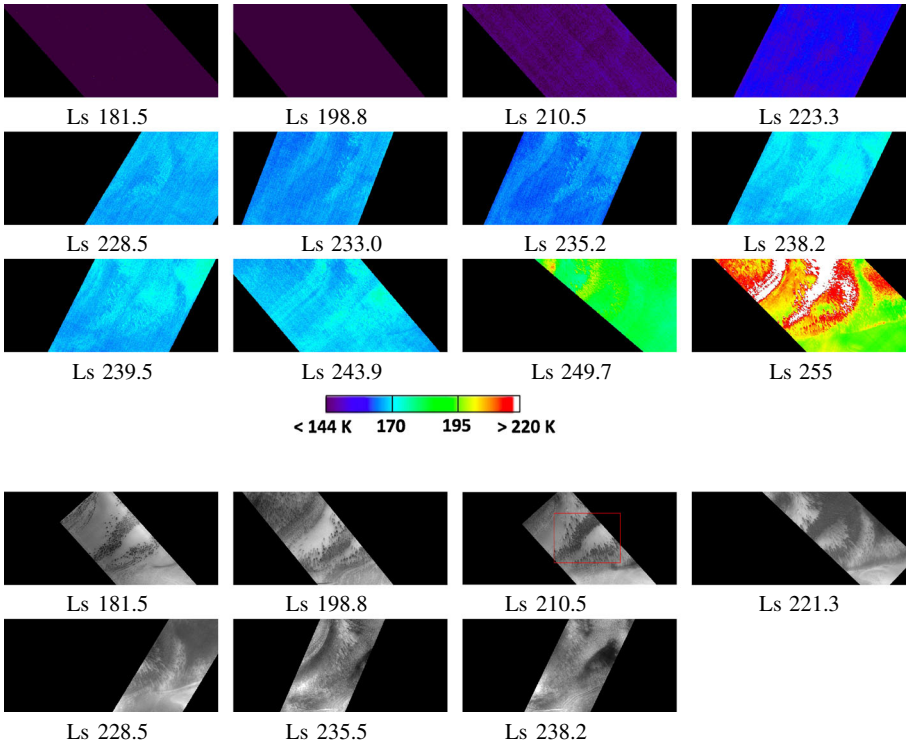

Figure 2. (top) Surface temperature as seen by THEMIS in the Manhattan Island region (–86N, 100E) during MY28 southern spring. (bottom) THEMIS visible images over the same area of Manhattan Island. CRISM image spatial extent (Figure 3) is identified by red line. Structures begin to appear in the temperature maps at Ls 210.5, while dark spots are already present since the beginning of spring. Warm areas correspond to high concentrations of dark spots.

2010]. The presence of H_2O ice can be monitored through its 1.28 and 1.5 diagnostic spectral bands.

[29] The spatial extent of the dark material cover remains poorly known at the meter scale and below. Small-scale irregularities due to surface roughness may lead to small-scale spatial mixtures of covered and uncovered areas within a single pixel. Intimate mixtures (at the pixel scale) could also result from a very thin layer (a couple of grains thick) of dark material deposited on top of CO_2 ice. Both mixtures can be difficult to distinguish with CRISM spectra. However, surface temperatures are expected to follow different behaviors, depending on the mixing style. The temperature of a spatial mixture will be driven by the warmest spots, whereas in the case of an intimate mixture (very thin layer of covering material), the temperature is expected to remain very close to T^{surf}_{cond} ($\pm$ a couple of Kelvins; see section 4.2).

3. Data Analysis

3.1. Manhattan Island

[30] Dark spots are already present in the first images of the region that were acquired after the end of the polar night (Ls 181.5; see Figure 2). As pointed out by previous studies [*Titus et al.*, 2007], CRISM data show that dark spots are correlated with the observed localized CO_2 ice signature decreases (Figure 3). Moreover, the areas where dark spots are the most concentrated show a typical "cryptic" signature with temperatures near 145 K, a low reflectance ($R_{1.33\mu m}$ = 0.25–0.30), and a weak CO_2 ice spectral signature as early Ls 193 (no available data earlier), consistent with the presence of a quasi-opaque layer of dark material on top of CO_2 ice. Areas that do not exhibit dark spots show stronger CO_2 ice spectral signatures and higher reflectance ($R_{1.33\mu m}$ = 0.4–0.5). In spite of albedo differences, the scene has homogeneous temperatures near 145 K.

[31] During the following days, fans become more pronounced and the CO_2 ice signature decreases. However, as shown by Figure 2, surface temperature remains at $\approx T^{surf}_{cond}$ until Ls 210. At Ls 210, structures begin to appear on surface temperature maps (above the noise level, which is about 3 K as stated in section 2.3). These structures with a temperature slightly over T^{surf}_{cond} correspond to the areas where the dark spots are the most concentrated. These areas are referred to as the "dark" areas in what follows, whereas the areas which show no or a low concentration of dark spots are referred to as the "bright" areas. After Ls 210, the surface temperature of the dark areas continues to increase. The spatial distribution of these "warm" areas remains unchanged during spring. Between Ls 210 and Ls 221, the number of dark spots increases in the bright areas and the dark material spreads all over the region. The CO_2 ice signature also exhibits a net decrease over the whole area. The temperature of the bright areas also increases. During the following days, dark spots continue to develop and the ejected material continues to spread over the region.

[32] Unexpectedly, the former dark areas show an increase in reflectance ($R_{1.33\mu m}$ = 0.35–0.40), as well as their CO_2 ice signature, around Ls 236 (Figure 3). The former bright areas exhibit the opposite behavior with a decrease

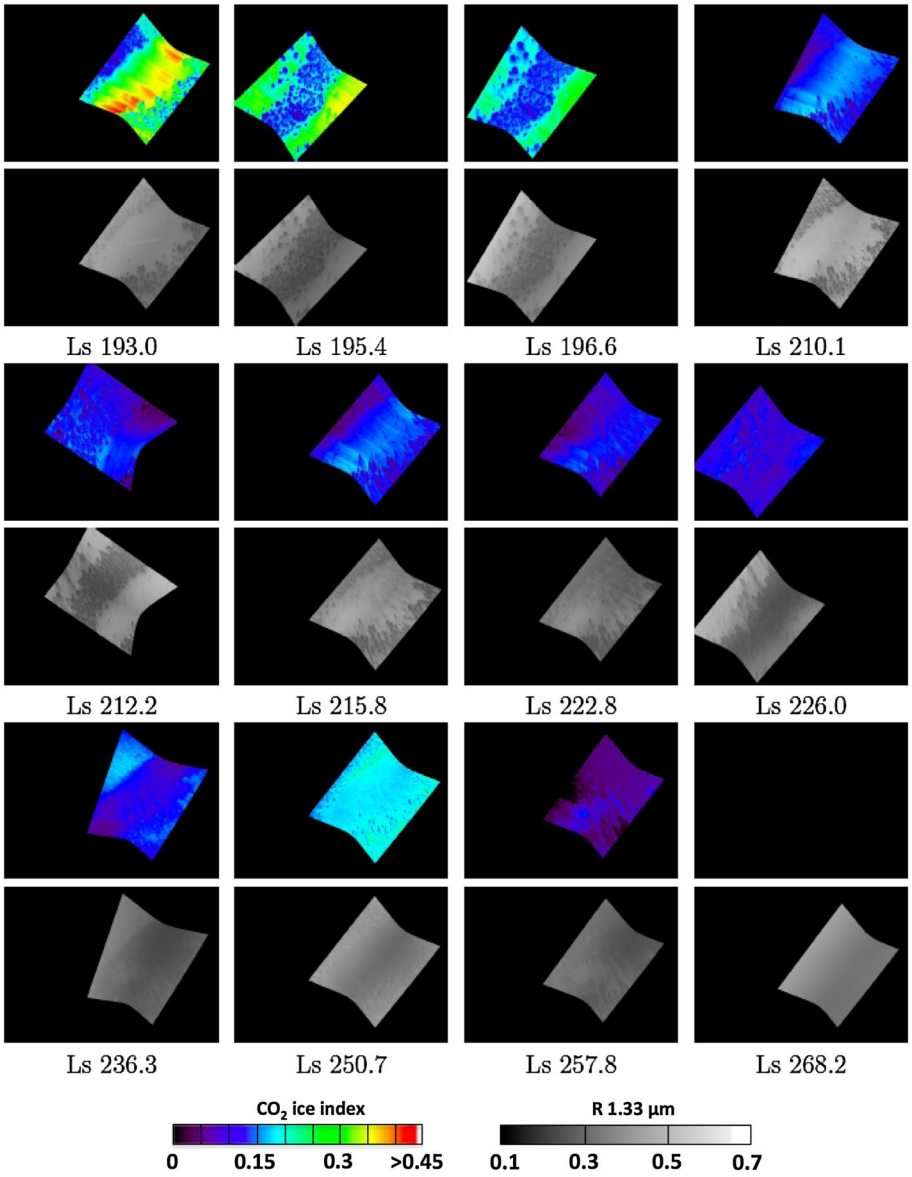

Figure 3. Figures with color scale show CO_2 ice spectral signature derived from CRISM data over Manhattan Island. Figures with gray scale show reflectance factor at 1.33 μm. Their spatial extent is identified by red line in Figure 2. CO_2 ice signature is directly correlated to the reflectance.

of both the reflectance ($R_{1.33\mu m}$ = 0.25–0.30) and the CO_2 ice signature. These trends are confirmed by THEMIS visible images acquired around the same time. THEMIS surface temperature retrievals do however not show a trend inversion; the surface temperature remains higher (around 170–175 K) in the former dark areas. We interpret this to be an effect of a small-scale spatial mixture of dark material-covered and dark material-free areas, the temperature being pulled by the warmest spots. The brightening of dark areas and darkening of bright areas are caused by the movement of some dark material from the darkest areas to the brightest ones.

[33] At Ls 250, the CO_2 ice signature is high for both areas. However, new dark spots have appeared, these latter being more concentrated where the first dark spots appeared at the beginning of spring. After Ls 257, some areas show no CO_2 ice signature and the surface temperature increases markedly: These areas are defrosted. This specific time is referred to as the "crocus date" (as in *Kieffer* [2007]). However, the surface temperature also exhibits an increase over areas that still show a clear CO_2 signature at the CRISM spatial resolution, which can be interpreted as the presence of both frosted and defrosted areas in the same pixel. This substantial temperature increase (mean temperature around 180 K, with high values at 210–230 K) can also result (at least partly) from the spreading of material that was just uncovered by CO_2 ice. CRISM spectra show that the entire region is defrosted by Ls 268. TES data confirm the slow increase of the surface temperature after Ls 210 and the beginning of the defrosting after Ls 250 (Figure 4).

3.2. Ithica

[34] The first THEMIS images over the region (Figure 5) were acquired rather late (Ls 226). However, CRISM images

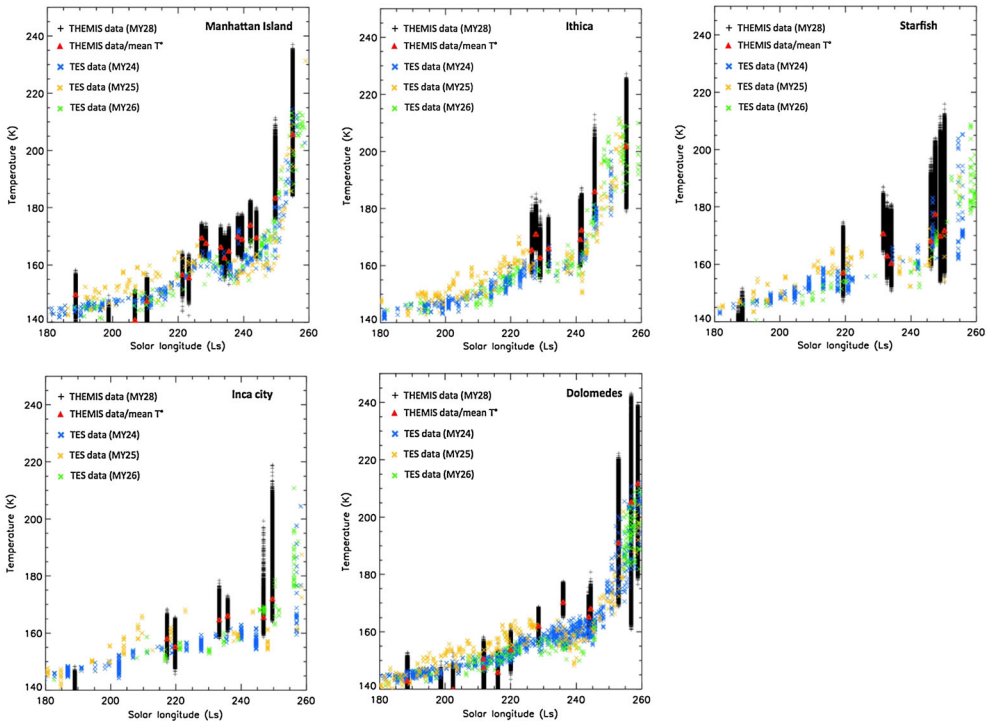

Figure 4. Evolution of the surface temperature over the different regions for MY28 as seen by THEMIS (spatial sampling of 100 m, black crosses). The vertical extension of the patterns shows the variability of temperature over the whole area. The red triangles indicate the "integrated" temperature over the whole area. THEMIS data have been acquired between 7 A.M. and 5 P.M. TES surface temperature retrievals (spatial sampling of 3 km) have been added for comparison: MY24 (blue crosses), MY25 (orange crosses), and MY26 (green crosses). A good correlation between both data sets can be observed. The high increase present after Ls 245–250 is due to the occurrence of defrosted patches.

(Figure 6) show that dark spots are already present on the first acquisition around Ls 185, as is the case for Manhattan Island. CRISM spectra of the dark spots show that some of the CO_2 ice is also already covered by a quasi-opaque dark material layer at that time. The bright areas show stronger CO_2 ice spectral signatures, but their reflectance remains rather low ($R_{1.33\mu m} \approx 0.35$). From Ls 185 to Ls 194 material accumulates over the ejection points and spreads over the whole area, resulting in decreased reflectance and CO_2 band strength (Figure 6). After Ls 194, however, the CO_2 ice spectral signature increases until the end of spring. Surface temperature retrievals, available after Ls 226, exhibit temperatures much above T^{surf}_{cond}, as was the case for Manhattan Island at the same period (Figure 5). Similar to Manhattan Island, structures can also be observed in the temperature maps; the dark areas (Figure 5) exhibit a much higher surface temperature than the bright ones (temperature contrast around 15–20 K in the available images). The surface temperature also increases between Ls 226 and Ls 242 (the increase seen at Ls 227.7 is attributed to a temporary increase of dust opacity). After Ls 245, the surface temperature rise seen in THEMIS data is consistent with the presence of defrosted spots. TES data exhibit a similar increase during the same period (Figure 4).

3.3. Starfish

[35] Starfish region exhibits dark spots as early as Ls 182, when the first CRISM data were acquired (Figure 7). THEMIS visible images show that a specific area, with a starfish form (albeit a three-legged starfish), exhibits a high concentration of dark spots, only sporadically present in the surrounding areas (Figure 8). Spectra acquired in the dark areas have a low reflectance ($R_{1.33\mu m}$ = 0.3–0.4) but clear CO_2 ice signature, which is consistent with a subpixel mixture of dark material-covered CO_2 ice and dark material-free CO_2 ice areas or an intimate mixture of CO_2 ice and dark material (typically a monolayer of dark material is present on top of CO_2 ice). The surface temperature is homogeneous across the scene and remains around T^{surf}_{cond} (Figure 8). The surrounding areas (bright ones), however, show a rather high reflectance ($R_{1.33\mu m}$ = 0.5–0.6) and a strong CO_2 ice signature.

[36] Between Ls 182 and Ls 206, the number and extent of dark spots increases not only in the dark areas but also in some specific locations of the bright surrounding areas. The reflectance and CO_2 ice signature decrease ($R_{1.33\mu m}$ = 0.26–0.28), to a minimum around Ls 199 which suggests an accumulation and spreading of dark material around the ejection point. At Ls 199, the dark areas are enlarged and covered by a nearly opaque layer of dark material. However, thereafter the reflectance and CO_2 ice band strength steadily increase. At Ls 219, THEMIS temperatures maps show a strong surface temperature contrast between the dark areas and the bright ones ($\Delta T \approx 20$ K; see Figures 8 and 4). Whereas the temperature of the dark areas keeps increasing, the temperature of the bright areas

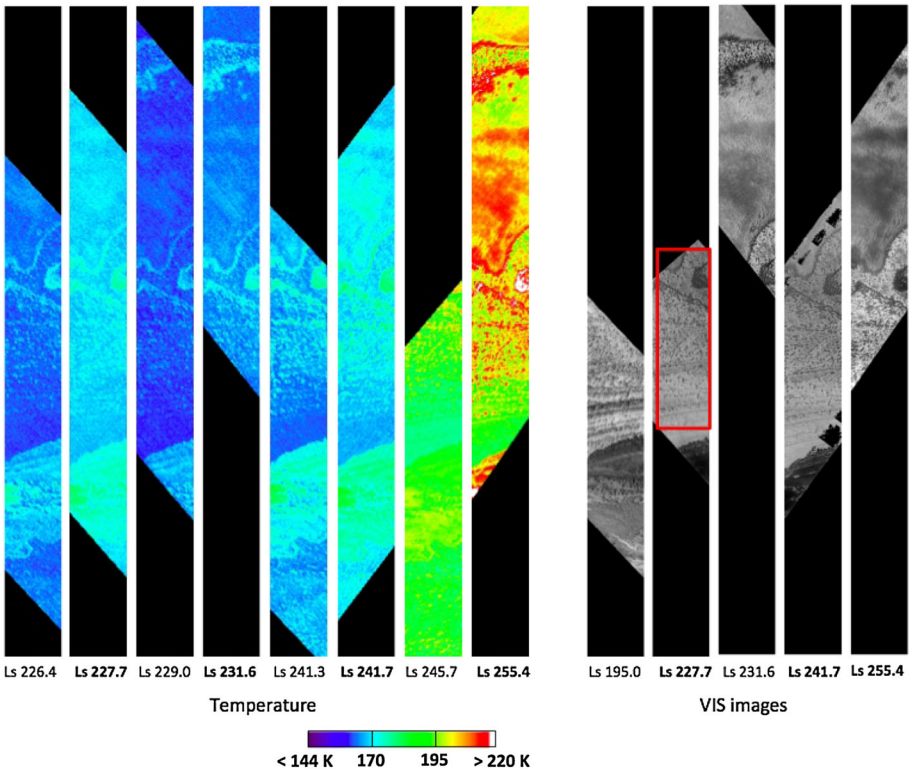

Figure 5. (left) Surface temperature as seen by THEMIS in the Ithica region (–85N, 179E) during MY28 southern spring. (right) THEMIS visible images over the same area of Ithica. CRISM image spatial extent (Figure 6) is identified by red line. Structures in the temperature maps are already present in the first image at Ls 226.4 and are correlated to dark areas.

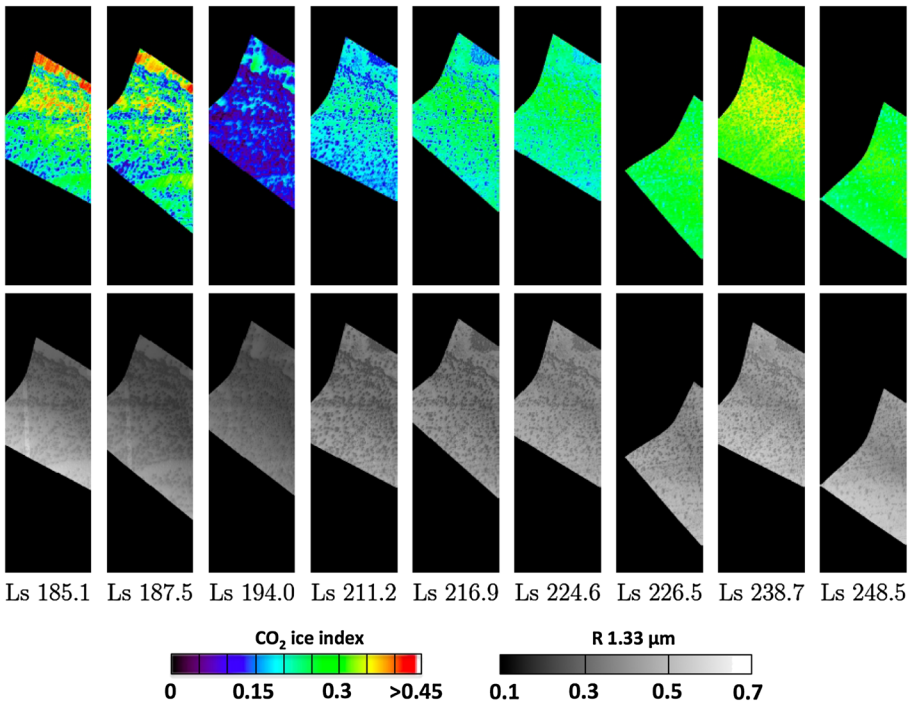

Figure 6. (top) CO_2 ice spectral signature derived from CRISM data over Ithica. (bottom) Reflectance factor at 1.33 μm. Their spatial extent is identified by red line in Figure 5. The CO_2 ice signature lowest values are reached at Ls 194 before a continuous increase.

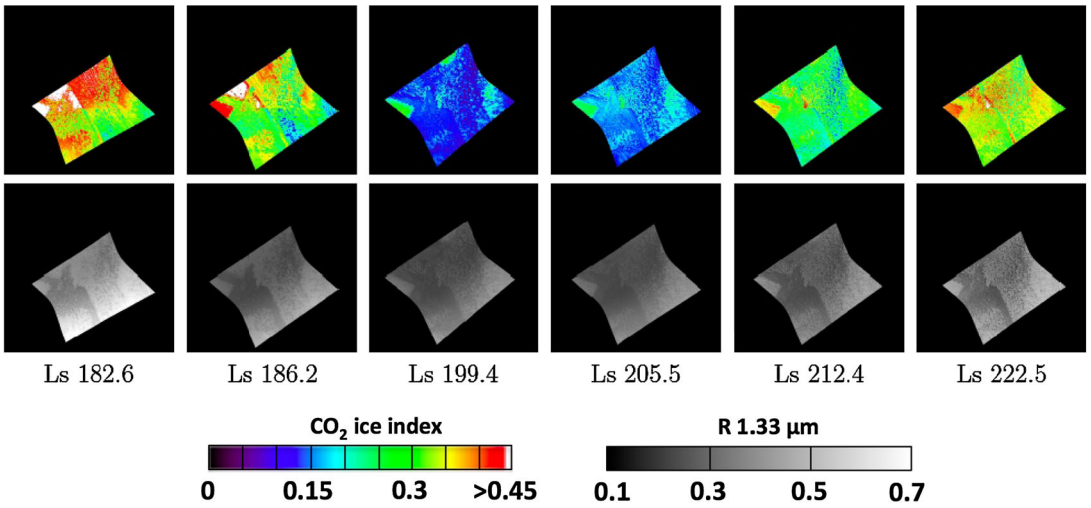

Figure 7. (top) CO_2 ice spectral signature derived from CRISM data over Starfish. (bottom) Reflectance factor at 1.33 μm. Their spatial extent is identified by red line in Figure 8. The CO_2 ice signature lowest values are reached at Ls 199.4 before a continuous increase.

increases slowly and remains between 150 and 160 K. This high contrast indicates that the ejected material tends to accumulate instead of spreading homogeneously over the region. The uniform and sporadic increase on THEMIS images at Ls 231 is attributed to a temporary increase of dust opacity.

[37] The temperature increases seen in THEMIS data after Ls 248 are most likely due to the presence of defrosted spots, since TES data exhibit a similar net increase a few days later. However, CRISM spectra acquired at Ls 252 show strong CO_2 ice signatures over the bright areas and spectral features consistent with subpixel mixing of CO_2 ice-covered (or defrosted)/uncovered spots over the dark areas. These latter exhibit rather high temperatures after Ls 248 (T_{surf} = 200–210 K), whereas temperatures of the bright areas remain typically below 160 K.

3.4. Inca City

[38] Similar to other regions, dark spots are also present in Inca City region when the first data were acquired at Ls 189. Dark spots are mostly present at the base of the dunes but can be found generally over the whole region, with highly variable concentration (see Figure 1 of the supporting information). Structures in the THEMIS temperature data are not

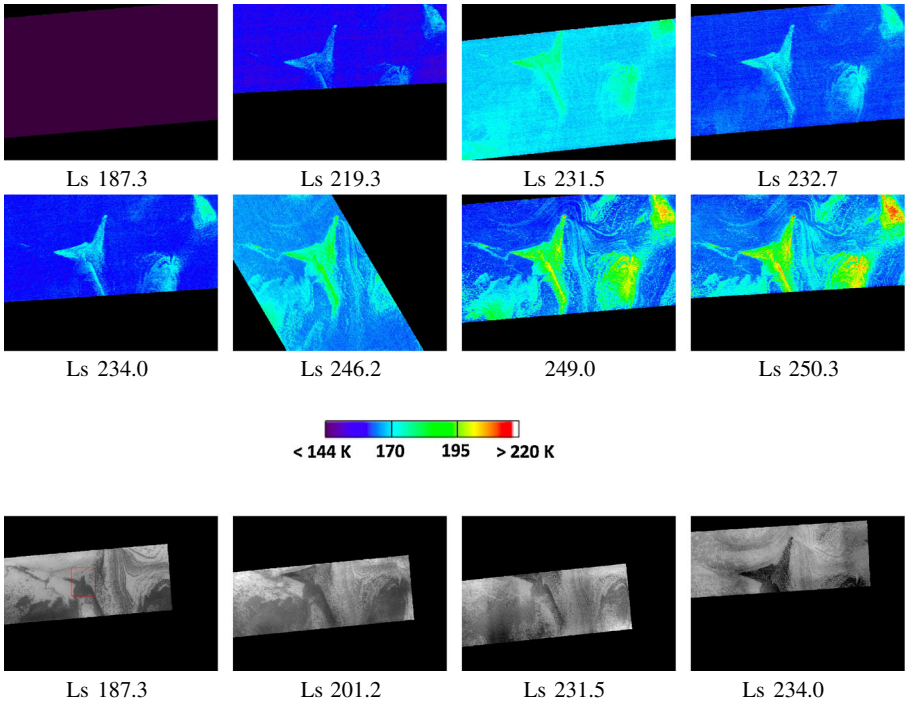

Figure 8. (top) Surface temperature as seen by THEMIS in the Starfish region (–84N, 241E) during MY28 southern spring. (bottom) THEMIS visible images over the same area of Starfish. No structures can be observed in the temperature maps before Ls 219.3, while dark spots are already present.

present at Ls 189, but a slight one can be observed at Ls 217.3, more prominent and accompanied by others in the following images. Similar to other regions, the surface temperature tends to increase slowly with time (see supporting information and Figure 4).

[39] Few CRISM data were available over the Inca City region. The otherwise strong CO_2 ice signature is greatly diminished over the dark spots at Ls 196 (see Figure 2 of the supporting information). The CO_2 ice signature tends to decrease between Ls 196 and Ls 206 in the bright areas but increase a little bit where dark spots are concentrated and is high but variable after Ls 206. A high increase of the temperature in the areas associated with the highest concentrations of dark spots can be observed after Ls 246. TES data exhibit a similar increase during the same Ls period in other years (Figure 4).

3.5. Dolomedes

[40] THEMIS visible data (Figure 3 of the supporting information) reveal that dark spot distribution generally corresponds to distinctive layers in the ice strata and that dark sports are aligned at different levels. The surface temperature remains around T_{cond}^{surf} until Ls 211.8, when structures begin to slightly emerge from the noise (Figure 4 of the supporting information). The surface temperature keeps increasing slowly, until Ls 253, when the areas with high dark spot concentrations exhibit a substantial temperature increase that can be interpreted as the occurrence of defrosted patches.

[41] CRISM data start at Ls 206, and data of dark spots generally exhibit a low reflectance ($R_{1.33\mu m}$ = 0.3–0.4), but the CO_2 ice signature always remains rather important, except in very few locations where dark spots are highly concentrated (Figure 9 and Figure 5 of the supporting information). The spectral signature of CO_2 ice increases until Ls 245, decreasing thereafter. Since surface temperature increases after Ls 211,even on patches with CO_2 ice signature, we interpret these data (between Ls 211 and Ls 253) as subpixel mixtures of dark material-covered CO_2 ice with the opaque patches pulling the surface temperature. This interpretation is consistent with ejected material spreading nonuniformly along the slopes.

3.6. Synthesis

[42] All five regions exhibit the same general behavior. Dark spots are already present in the first images taken after the end of the polar night (around Ls 180–190). CRISM data generally show that the dark areas increase in size between Ls 180 and Ls 200 with a decrease of the CO_2 ice signature and the reflectance until Ls 200–210 (Figure 9). This is consistent with ejected material becoming more abundant, accumulating around the ejection points until becoming opaque layers of dark material and spreading over the area. However, the temperature remains homogeneous and consistent with the condensation point until ≈ Ls 200–210. Then elevated temperatures corresponding to the highest concentrations of dark spots begin to appear on THEMIS thermal images. The temperature of these regions increases slowly with time, with the darkest areas showing a greater increase (contrast of 5–20 K; see Figure 4). The CO_2 ice signature however increases after Ls 200–220 (in agreement with *Pommerol et al.* [2011]), until defrosting occurs

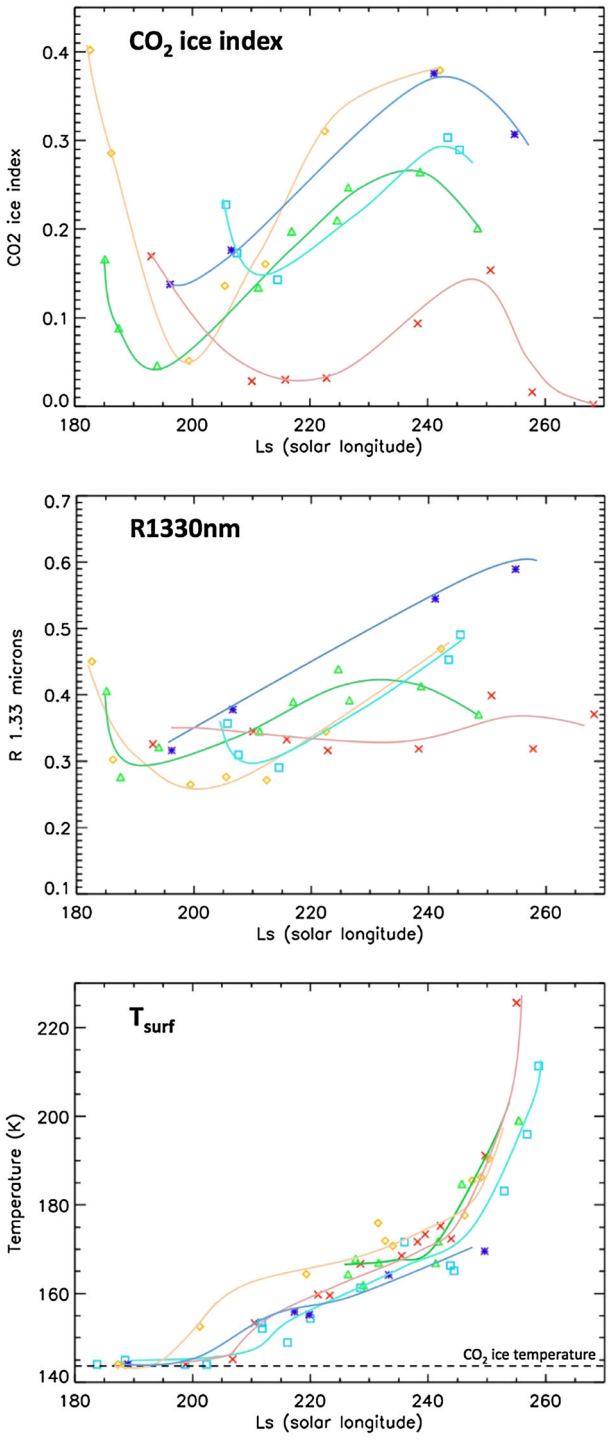

Figure 9. (top) Temporal evolution of the CO_2 ice index, (middle) the reflectance factor at 1.33 μm, and (bottom) the surface temperature over a dark spot for the different regions (data taken over a single pixel). Red crosses: Manhattan Island; orange diamonds: Starfish; green triangles: Ithica; light blue squares: Dolomedes; dark blue stars: Inca City.

(Figure 9). The first defrosting spots appear around Ls 245 in the areas where dark spots where highly concentrated while CO_2 ice signature can still be observed, which is consistent with subpixel mixing of defrosted and frosted areas. In particular, THEMIS data highlight that defrosting spots always occur a bit earlier on dark areas than on bright ones.

4. Modeling and Data Interpretation

[43] In order to better understand THEMIS thermal observations, we developed numerical tools to simulate the thermal behavior of CO_2 ice covered by a layer of dark material. We describe in the next section the model, then we summarize the general behavior of such covered layer of CO_2 ice. Finally, we use the model to retrieve quantitative data about the ejected material layer.

4.1. Model Description

4.1.1. General Description

[44] To simulate the surface temperature evolution of CO_2 ice covered by some dark material, we use a simplified version of *Pilorget et al.* [2011] model. The latter is an extension from a 1-D version of the General Circulation Model (GCM) from Laboratoire de Meteorologie Dynamique [*Forget et al.*, 1999] and simulates the detailed seasonal evolution of a layer of CO_2 ice at a given location on Mars by solving heat exchange, radiative transfer, and mass evolution equations in the CO_2 ice as well as in the soil.

[45] We use here a simplified version of this model, i.e., without the radiative transfer, by assuming that the dark material layer is opaque. A finite volume approach is used to solve the equations, with a time step of 0.001 Martian day (89 s). The model takes into account the solar flux (0.1–5 μm), the incident thermal flux, the thermal emission, the sensible heat flux, the geothermal heat flux, and the latent heat flux when there is a phase transition (CO_2 sublimation/condensation).

[46] The simulation starts from the time of material ejection (initially set to be Ls 173). At that time, a thermal profile is assumed within the CO_2 ice (see section 4.2) and a layer of dark material is set on top of CO_2 ice, initially at the temperature of CO_2 sublimation ($T_{\mathrm{cond}}^{\mathrm{surf}}$). Only the period where CO_2 ice is present is simulated (the reservoir of CO_2 ice remains infinite during that period); thus, no prediction is made for the crocus date.

4.1.2. Vertical Grid

[47] We simulate in what follows the thermal behavior of dark material layers with thermal inertias ranging from 50 to 150 SI, which corresponds to grain sizes from a few tens of micrometer to a few hundreds of micrometer at this temperature [*Piqueux and Christensen*, 2011]. The dark material layer thickness can range from 200 μm to a few millimeters.

[48] The vertical computational grid used in the model is a static layer grid where individual layers have distinct thermal and optical properties. The most appropriate one for thermal conduction in soil problems is an irregular, stretched grid since higher resolution is required near the surface, whereas a much coarser grid suffices for deeper layers. This leads to defining layers of increasing extent with increasing depth, following power laws. In our case, the midlayer depth distribution (where the temperature is computed at each time step) follows

$$d(i) = 2.10^{-5}\ (1.2)^{i-1/2} \tag{3}$$

with $d(i)$ the depth of the midlayers in meter, such that the dark material is represented by typically a few tens of thin opaque layers.

4.1.3. Thermal Conduction in the Dark Material and in the Ice

[49] Thermal conduction is here considered as a one-dimensional process. Temperature T of the soil is thus a function of time t and depth z, which must satisfy the following equation:

$$\rho\ C_{\mathrm{p}} \frac{\partial T}{\partial t} = \frac{\partial}{\partial z}\left(\lambda \frac{\partial T}{\partial z}\right) \tag{4}$$

where ρ is the density (kg.m^{-3}), λ the conductivity (J.s^{-1}.m^{-1}.K^{-1}), and C_p the specific heat (J.kg^{-1}.K^{-1}).

[50] Thermal conduction in the soil is computed as follows:

[51] 1. Time integration is done via an implicit (first order) Euler scheme which approximates the differential equation $\mathrm{d}T(t)/\mathrm{d}t = F(T, t)$ as:

$$\frac{T^{(i+1)} - T^{(i)}}{\delta t} = F(T^{(i+1)}, t^{(i+1)}) \tag{5}$$

where superscripts denote time levels and δt the time step.

[52] 2. The lower boundary condition (no outgoing or incoming heat flux) is included as such in the solver, but the upper boundary condition (balance of heat fluxes through the surface and cooling thereof) is not. Surface temperature is technically linked to atmospheric and ground processes which are coupled. Rather than solving the coupled problem, it is uncoupled in a way that allows one to solve atmospheric and ground processes separately. The essential feature of the artificial uncoupling is that the atmospheric problem is first solved, yielding in the processes the value of surface temperature $T_{\mathrm{surf}}^{(i+1)}$ at time $t^{(i+1)}$, which is then used as an input boundary condition for the soil heat diffusion problem.

4.1.4. Algorithm

[53] In the case of a clean CO_2 ice slab (with photon path lengths of a few tens of centimeter), most of the solar flux penetrates through the ice and reaches the underlying regolith where it is (partially) absorbed. However, if an opaque layer is deposited on top of the CO_2 ice slab, thermal conduction makes the thermal wave propagate very quickly down to the CO_2 ice. We therefore first need to convert the energy in excess to the amount of CO_2 that sublimates before computing the thermal conduction in the underlying layers. Thus, heat, radiation, and mass evolution need to be coupled. The algorithm that is used is the one developed by *Pilorget et al.* [2011]. It consists of depositing the energy in the first opaque layer, then doing a loop with the following processes:

[54] 1. calculate the thermal conduction within the dark material layer, as well as in the CO_2, and derive the temperature profile;

[55] 2. find the layer of CO_2 ice where the excess (or deficiency) of energy is the highest compared to the

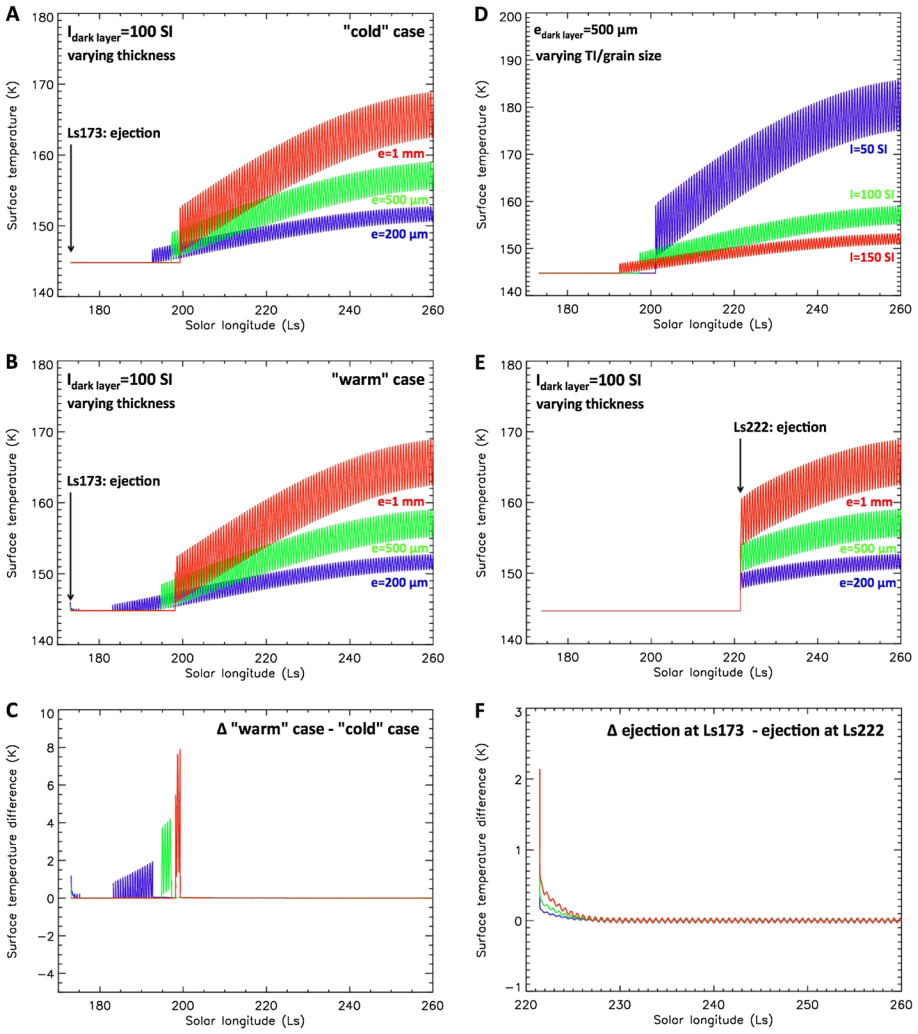

Figure 10. (a) Evolution of the surface temperature for a dark material layer of thickness e is covering a CO_2 ice slab. Blue: e = 200 μm, green: e = 500 μm, and red: e = 1 mm. The dark material layer is deposited on top of the CO_2 ice at Ls 173. Its thermal inertia is set at 100 SI. Thermal inertia of the CO_2 ice is set at 1000 SI. We consider here a flat terrain at a latitude of –86.3°. The temperature within the ice is set at $T_{\mathrm{cond}}^{\mathrm{surf}}$ at the beginning of the simulation ("cold" scenario). CO_2 ice always remains available in these simulations. (b) Same except that the temperature within the ice is set at the sublimation temperature at the cryostatic pressure at the beginning of the simulation ("warm" scenario). (c) Surface temperature difference between the "warm" and "cold" scenarios. (d) Evolution of the surface temperature for a dark material layer of thickness 500 μm and thermal inertia I covering a CO_2 ice slab (cold scenario). Blue: I = 50 SI, green: I = 100 SI, and red: I = 150 SI. The dark material layer is deposited on top of the CO_2 ice at Ls 173. We consider here a flat terrain at a latitude of –86.3°. (e) Same as Figure 10a except that the dark material layer is deposited on top of the CO_2 ice at Ls 222.2. (f) Surface temperature difference between the case where the ejection occurs at Ls 173 and the case where the ejection occurs at Ls 222.

sublimation point (the top CO_2 ice layer in contact with the dark material in our case). It is the layer where sublimation (or condensation) is the most likely to occur;

[56] 3. compute the latent heat related to this sublimation (or condensation);

[57] 4. calculate the new thermal conduction coefficients and compute the new temperature profile;

[58] 5. return to step two as long as there is still an excess of energy (or a deficiency) in the specified conditions.

[59] Calculating processes this way guarantees that the thermal conduction is computed using realistic temperatures in the CO_2 ice that are never higher than the sublimation point. In what follows, the dark material layer is assumed to be porous, so that sublimated CO_2 can escape through the pores.

4.2. General Thermal Behavior of Dark Material-Covered Areas

[60] The covering of the CO_2 ice by an opaque layer of ejected material prevents solar flux penetration into the ice. The energy is absorbed by the covering layer or reflected back, and the basal sublimation stops. Modeling results show that the surface temperature increases slowly with time, much above the CO_2 condensation temperature, even for thin layers of dark material (Figure 10). However, the surface temperature remains much lower than in the case

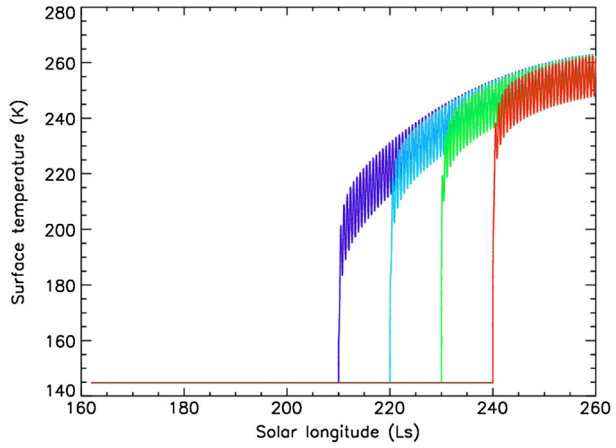

Figure 11. Evolution of the surface temperature in case the crocus date (complete removal of CO_2 ice) occurs at Ls 210 (dark blue), Ls 220 (sky blue), Ls 230 (green), and Ls 240 (red). Soil thermal inertia is set at 200 SI. We consider here a flat terrain at a latitude of –86.3°.

where the CO_2 ice has completely sublimated (Figure 11). Surface temperature increase is limited by the temperature at the interface between the dark material layer and the CO_2 ice that remains at the sublimation temperature (we neglect the effect of the grains weight on the pressure at the interface with CO_2 ice and assume that CO_2 ice is in equilibrium with the atmosphere). Diurnal variations of a few Kelvins can be noted.

[61] Figure 10a shows that for a dark material layer of a given thermal inertia, the thickness of the layer has an important impact on the surface temperature, both on the increase as a function of Ls and the diurnal amplitude (which is small, a few Kelvins typically, compared to the overall increase, around 10 to 25 K in the present case). Interestingly, we can notice that in the case of an early dark material ejection (Ls 173), some CO_2 ice condensation on top of the dark material layer occurs during the first days (≈ a few millimeters). Indeed, just after the end of the polar night the day duration remains quite short; thus, CO_2 ice condenses during the night on the low thermal inertia dark material layer. Once the solar flux becomes high enough (as well as the day duration), the CO_2 ice begins to sublimates and disappears around Ls 190–200. Figure 10a shows that the thicker the layer, the greater the cooling insulation. However, these simulations assume that only one ejection occurs (at Ls 173) and that the dark material layer is already opaque, which is likely not the case (in reality several ejections might occur during that period, progressively increasing the layer thickness). Therefore, the timing of the end of sublimation of the potential layer of CO_2 ice on top of the dark material layer should be considered as an upper bound. Surface temperature will however remain close to $T_{\mathrm{cond}}^{\mathrm{surf}}$ before ≈ Ls 200, as the solar flux is very low.

[62] When there is no dark material covering on the CO_2 ice (before the first ejection), the solar flux penetrates into the ice and reaches the regolith underneath, which warms up to the CO_2 ice sublimation temperature. Because the temperature remains at $T_{\mathrm{cond}}^{\mathrm{surf}}$ at the surface, whereas it increases at the regolith/ice interface, the temperature within the ice increases, driven by thermal conduction and absorption of the solar flux to a lesser extent [*Pilorget et al.* 2011, Figure 8]. Therefore, the temperature within ice that is covered by dark material can be much warmer than the surface condensation temperature. Figure 10b shows that the temperature within the CO_2 ice only affects the CO_2 ice recondensation process. The energy kept within the ice, in the "warm" CO_2 ice scenario, limits CO_2 ice recondensation during the night; consequently, sublimation of CO_2 and temperature increase occur earlier than if all ice were at $T_{\mathrm{cond}}^{\mathrm{surf}}$. However, ultimate surface temperature remains the same in both scenarios after CO_2 ice has gone (around Ls 200).

[63] Results of a numerical model [*Piqueux and Christensen*, 2011] have shown that in the case of uncemented particulate soil, an estimate of effective particle size could be inferred from the thermal inertia for a given temperature. At 150 K, a thermal inertia of 50 SI roughly corresponds to a grain size of ≈45 μm, 100 SI to ≈200 μm, and 150 SI to ≈700 μm. Assuming that this layer of dark material is opaque, we can evaluate the impact of its thermal inertia, thus of the grain size, on the surface temperature (Figure 10d). As the thermal inertia decreases, the surface temperature increases due to the presence of a layer of dark material, similar to the effect of a normal soil. Importantly, the presence of some CO_2 ice under the dark material layer exerts significant temperature control. When completely absent surface temperatures are much higher than in the case of thin dark material cover from ejection (Figure 11 versus Figure 10a).

[64] Regardless of when the ejection happens, the surface temperature transient state is very short and after a few hours the temperature is less than 1 K from the steady state (Figures 10e and 10f). As a result, the surface temperature at the surface of a dark material layer covering CO_2 ice depends on its location, Ls, local hour, thickness of the layer, and of its thermal properties (that relate to the material grain size) and is quasi-independent of the ejection occurrence and the initial temperature conditions within the ice (Figures 10e and 10f). It can thus be used to retrieve quantitative estimates about this dark material layer thickness.

4.3. Dark Material Thickness Retrieval

[65] Retrievals of the dark material thickness can be obtained by comparing the THEMIS temperatures with modeling results (for the same Ls and local time, assuming an homogeneous cover and a flat terrain). Figure 12 shows that dark material layer thicknesses of a few hundreds of micrometer to a couple of millimeters are expected for assuming a typical thermal inertia of 100 SI. Results obtained with a lower thermal inertia (50 SI) give results in the range of a few hundreds of micrometer, whereas those obtained with a higher thermal inertia (150 SI) are in the range of a couple of millimeters typically. These results are consistent with *Kieffer et al.* [2006], *Langevin et al.* [2006], and *Piqueux and Christensen* [2008] estimates within uncertainties. These retrievals show no appreciable increase of the dark material thickness between Ls 210 and Ls 245–250, although small changes in thickness are permitted by the data. The extreme temperature increase observed after

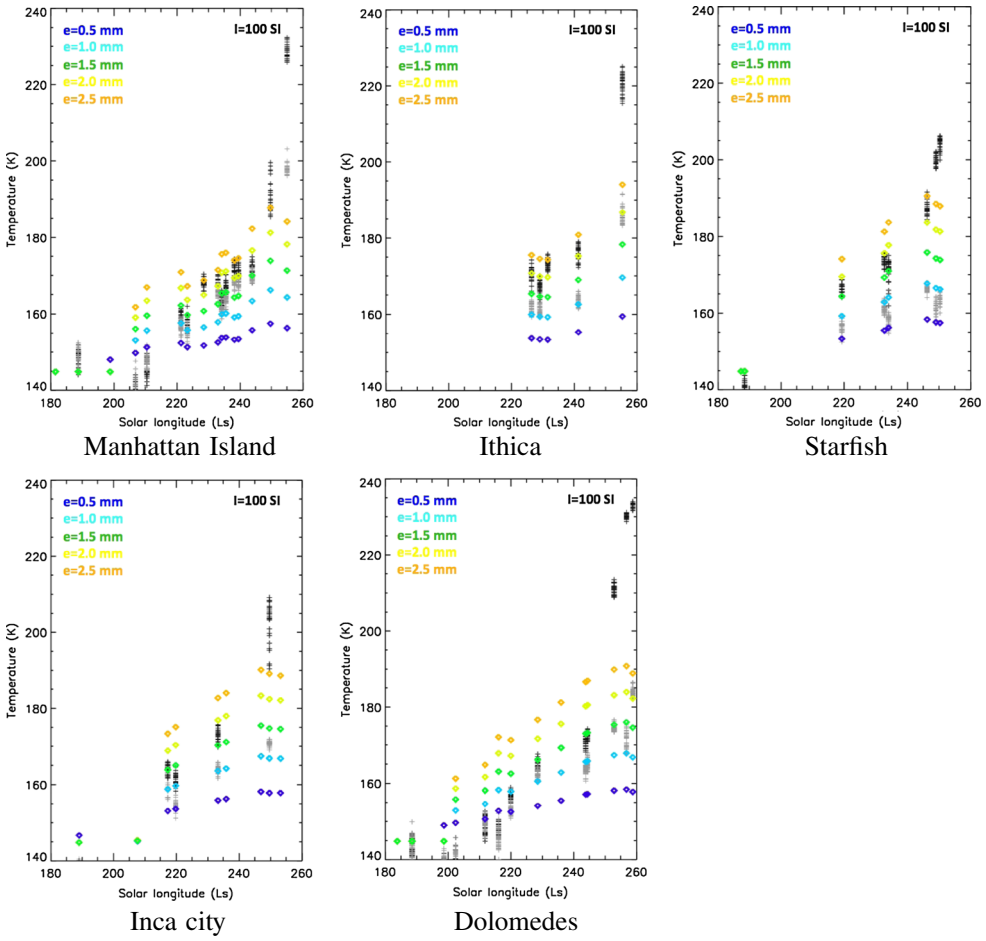

Figure 12. THEMIS surface temperature retrievals for image "dark" spots (5 × 5 pixels, black crosses) and "bright" spots (5 × 5 pixels, gray crosses). For each THEMIS acquisition, temperatures computed at the same time (Ls and local hour) with the numerical model have been added for comparison, assuming that the pixel is 100 % covered by the dark material. The dark material thermal inertia is set at 100 SI. The high temperature increase around Ls 250 in the data is due to the beginning of defrosting. This increase cannot be seen in the simulations since CO_2 ice always remain available in the model.

Ls 245–250 is due to complete defrosting in some locations (at subpixel or pixel scale).

[66] Surface temperature retrievals in conjunction with CO_2 ice absorption depth decreases suggest entire region is covered with material, although of varying thickness. These results are discussed in section 5.1.

[67] Subpixel mixing, as well as slope effects, may affect the surface temperature and thus the thickness retrievals. We conducted a sensitivity study for these two parameters. Results show that the temperature increase on a 15°N-oriented slope is limited to a few Kelvins (+6 K in the case of a material layer of 500 μm and I = 100 SI). The thickness retrieval may in that case be underestimated by a few tens of percents. In the case of subpixel mixing (CO_2 ice with and without dark material cover), the temperature of the dark material-covered part may be underestimated (up to 13 K for a 50–50% mixture and a measured temperature of 169 K; see Figure 13), while the temperature of the uncovered part remains at T_{cond}^{surf}. In case of subpixel mixing, dark material cover could be thicker in those places that are covered. However, at the pixel scale, the total amount of material remains in the same range.

5. Discussion

5.1. Surface Evolution

[68] While CRISM data show a decrease of both surface reflectance and the CO_2 ice signature in early Southern spring, no increase of temperature is observed in THEMIS data before Ls 200–210. During that period, the development of dark spots and the accumulation of dark material around the ejection points suggest that several ejections occur. After Ls 200–210, surface temperature increases above T_{cond}^{surf} where the dark spots the most concentrated. The results of the numerical model are consistent with these observations. The presence of an opaque layer of dark material on top of the CO_2 ice is expected to lead to temperatures above T_{cond}^{surf}, typically 5 to 30 K, depending on the Ls and the layer properties (thickness and thermal inertia). This temperature rise is however not expected to be significant before Ls 200–210, because of the low insolation, which is in full agreement with THEMIS and TES observations. As revealed by the model results (Figures 10a and 10c) and in agreement with observations (Figure 9), CO_2 ice recondensation on top of the ejected material could also occur

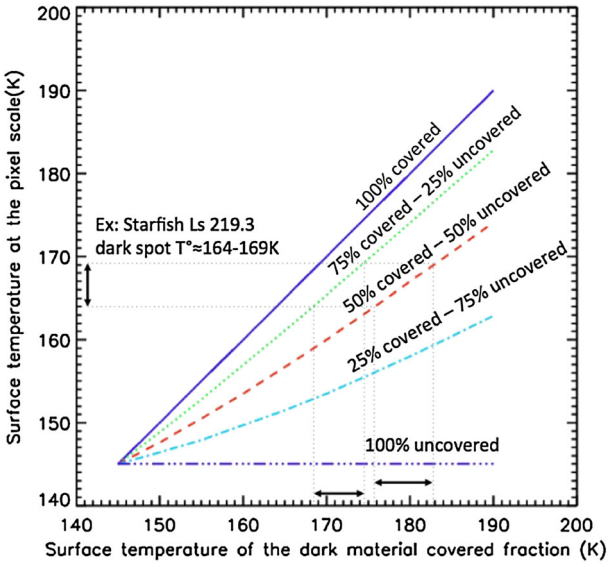

Figure 13. Temperature seen by THEMIS in band 9 (pixel scale) for a spatial mixture of 25% CO_2 ice and 75% CO_2 ice covered by dark material (dotted green line), a spatial mixture of 50% CO_2 ice and 50% CO_2 ice covered by dark material (dashed red line), and a spatial mixture of 75% CO_2 ice and 25% CO_2 ice covered by dark material (light blue mixed line). CO_2 ice and dark material emissivities are taken at 1. CO_2 ice fraction is assumed to have a temperature at T_{cond}^{surf}. The warmest fraction within the pixel (areas where CO_2 ice is covered by dark material) drives the temperature at the pixel scale. The example of a spot over Starfish at Ls 219.3 has been added in the figure. In this example, the surface temperature of the covered fraction may reach 169–174 K (75% covered case) and 176–182 K (50% covered case).

at the very beginning of spring. Afterward, the temperature is expected to increase slowly above T_{cond}^{surf} but to remain much below the expected temperature of fully defrosted soil, consistent with both THEMIS and TES data sets. CRISM spectra confirm the presence of CO_2 ice throughout spring. Temperature elevation due to subpixel defrosted areas is ruled out at these early times (Ls 200–230), since the complete defrosting only occurs much later (after Ls 250) on these terrains. HiRISE/CRISM coupled observations also exclude this hypothesis [*Pommerol et al.*, 2011]. CRISM spectra also show no evidence for the presence of a thermally thick layer of water ice (typically more than a few tens of microns) on top of the CO_2 ice, consistent with results from *Appéré et al.* [2011]. Model results also show that small diurnal variations of a few Kelvins are expected when some material lays on top of the CO_2 ice, in full agreement with *Kieffer et al.* [2000] who observed similar diurnal variations in TES data over the cryptic region.

[69] In addition to a net increase of temperature over the dark spot concentrations, THEMIS data highlight a slow increase of the surface temperature over the different regions. The presence of dust in the atmosphere could increase homogeneously the measured temperatures by a few Kelvins (see section 2.3). However, the expected increase is not sufficient to explain the observations. TES surface temperature retrievals over the regions with a cryptic behavior and the perennial cap also show that both kinds of regions exhibit a different behavior (Figure 14), despite their proximity. The regions with a cryptic behavior exhibit a net temperature increase in spring, whereas the perennial cap remains at temperatures around T_{cond}^{surf} (with some small increase likely due to the effect of atmospheric dust). CRISM data also highlight a general decrease of the CO_2 ice signature before ≈ Ls 200–210 over the studied areas. We therefore interpret this temperature increase to be due to the presence of material on top of CO_2 ice, coming from the spreading of the ejected material over the area (from concentrated areas of dark spots or from isolated dark spots).

[70] Dark material thickness ranges from a few hundreds of microns to a few millimeters, with temporal and spatial variations, under modeling assuming plausible material thermal inertia of 100 SI. Thermal inertia is, however, likely not homogeneous. The coarser grains ("high" thermal inertia) are expected to remain closer to the ejection point, whereas the smaller ones ("low" thermal inertia) can spread more widely over the area, which would therefore suggest that the darkest areas may be covered by a "high" thermal inertia layer of a couple of millimeters, whereas the brightest ones may be covered by a "low" thermal inertia layer of a few hundred of microns. This could be better constrained using wind estimates and simulations of possible aeolian transport in these regions.

[71] After ≈ Ls 200, CRISM data highlight an increase of the CO_2 ice signature, suggesting that no more dark material is ejected (dark spot occurrence late spring is however sometime observed, as in Manhattan Island, for example). If dark material sinking through the ice might occur, the THEMIS temperature retrievals suggest that (at least) some material remains on top of the ice, leading to temperatures above T_{cond}^{surf}. We therefore propose that after the material ejection, which leads to some

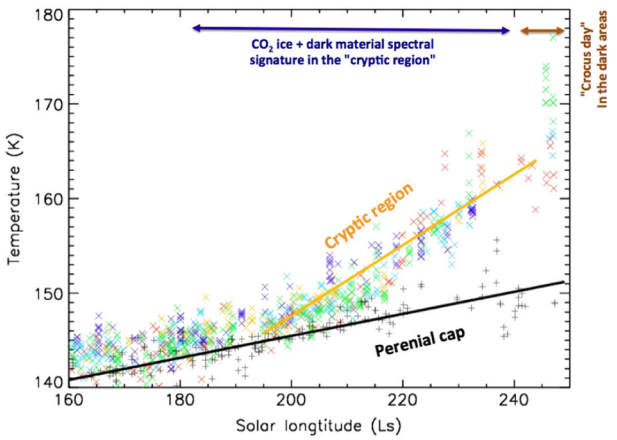

Figure 14. Evolution of the surface temperature as seen by TES over MY24 for the five studied regions exhibiting a cryptic behavior (colored crosses) and the perennial cap (black crosses). Red: Manhattan Island, orange: Starfish, green: Ithica, light blue: Dolomedes, and dark blue: Inca City. Grain size difference (and thus emissivity) could explain an offset between both regions but not the temperature increase seen observed in the regions exhibiting a cryptic behavior.

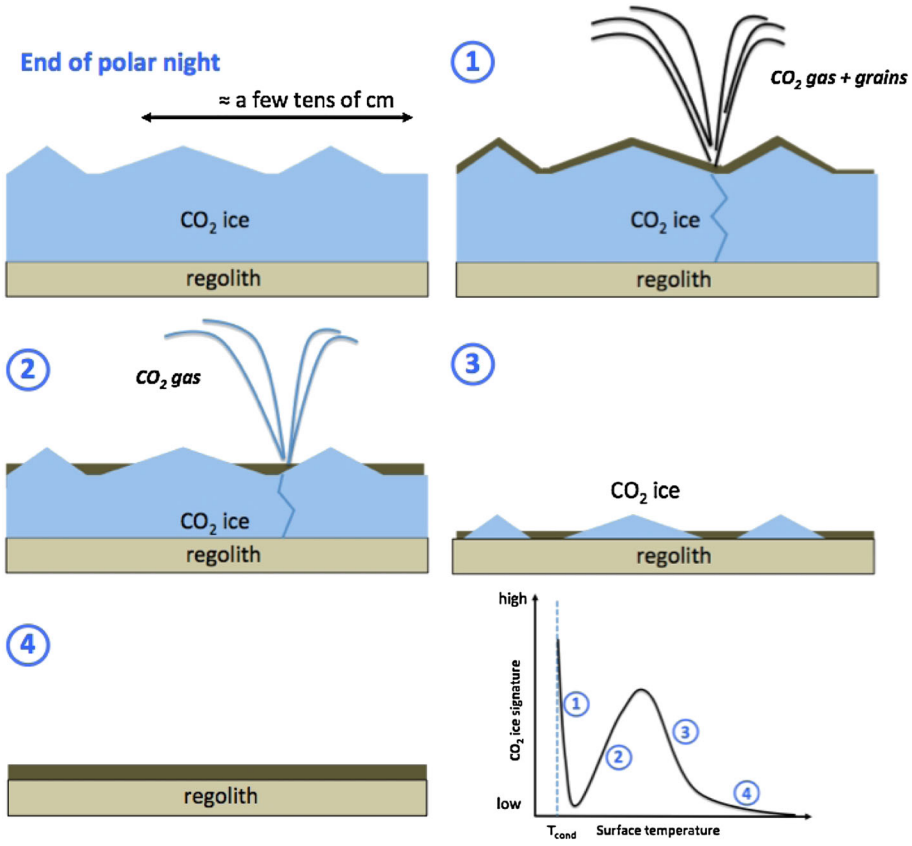

Figure 15. Illustration of the temporal and spatial evolutions of the dark material cover. (1) The ejected material covers homogeneously the CO_2 ice (at scales smaller than the dark spot). The CO_2 ice signature decreases rapidly. The surface temperature increases with the solar flux. (2) Wind and surface roughness create some heterogeneities in the cover, leading to an increase of the CO_2 ice signature, while the temperature also increases. Basal sublimation continues since only a fraction of the surface is covered by opaque material. (3) Patches of defrosted soil developed around Ls 245–250, leading to a rapid increase of the temperature and a decrease of the CO_2 ice signature, until CO_2 ice has disappeared (4).

rather homogeneous spatial covering, wind and small-scale irregularities in the surface (surface roughness) tend to make this material accumulate in specific locations, leading to some subpixel spatial mixtures (in agreement with *Pommerol et al.* [2011] and S. Douté, Monitoring atmospheric dust spring activity at high southern latitudes on Mars using OMEGA, submitted to *Icarus*, 2013). Ejected CO_2 gas could also recondense on the surface [*Titus et al.*, 2007b; *Pilorget et al.*, 2011], which would cause an increase of the CO_2 ice signature and a brightening of the surface (small grains). This conceptual model is summarized in Figure 15.

[72] At the end of spring, THEMIS data show that defrosted patches (at least at the subpixel scale) occur first where dark spots are the most concentrated. For example, THEMIS data show that defrosted patches occur between Ls 245 and Ls 249 where dark spots are the most concentrated in Manhattan Island, whereas they only occur around Ls 260 for surrounding areas. Other regions exhibit the same behavior. An accumulation of dark material, with a low albedo, on top of the ice seems to slightly increase the sublimation rate of the ice. Experimental results would be needed to confirm these behaviors. These effects are nonetheless limited and cannot explain the important recession rate asymmetry between the cryptic and the noncryptic areas [*Kieffer et al.*, 2000; *Colaprete et al.*, 2005], which is more likely due to smaller-grained CO_2 ice and/or higher-CO_2 snow/H_2O inclusions in the noncryptic areas.

5.2. Implications for the Surface Properties

[73] As shown in previous sections, the venting process is responsible for transporting some material from below the CO_2 ice slab to the surface (a few hundreds of microns to a few millimeters). The grain size distribution of the ejected material is likely to be different from its source, because the ejection process might not be strong enough to lift and transport the larger grains. Furthermore, the deposition rate of the grains after ejection highly depends on their size, with longer fallout times for smaller particles [*Kieffer*, 2007]. Thus, we suggest that at the end of spring, when the CO_2 ice is removed, the regolith layer grain size distribution is likely to be heterogeneous with the upper layers made of finer material than the lower layers. This process may therefore be responsible for the progressive transport of the finer fraction of the regolith to the surface, which would tend to lower the thermal inertia with regards to surrounding regions where venting does not occur. This is consistent with *Kieffer et al.* [2000] which reported that the "cryptic"

region, where dark spots are highly concentrated, roughly corresponds to the low-thermal inertia area observed by *Paige and Keegan* [1994].

[74] In addition to polar latitudes, this kind of process may also occur at lower latitudes. The occurrence of slab ice (with photon path lengths of a few tens of centimeter) has been reported broadly on Mars [*Langevin et al.*, 2007], up to 45°S latitude, and basal sublimation should occur in these areas [*Pilorget et al.*, 2011]. Following the scenario described in the previous paragraph, CO_2 ice basal sublimation related processes may be responsible for the mobilization of the relatively small volumes of regolith material needed to obscure the high-thermal inertia/bedrock surfaces (typically a few hundreds of microns), contributing to the lack of in-place bedrock poleward of 50° latitude [*Edwards et al.*, 2009] and substituting for or adding to the effects of active layer processes [e.g., *Kreslavsky et al.*, 2008]. This process may have been more efficient in the past when obliquity was higher ($\approx$ 45°) and CO_2 ice seasonal caps extended to up to 30° latitude. Material and gas ejection through CO_2 ice basal sublimation may therefore constitute an important and underestimated regolith mobilization process of the Martian surface at midlatitudes, to be determined with future study. In particular, experimental work would be needed to confirm the efficiency of such process and give constrains on their timescale.

6. Conclusion

[75] Previous studies had reported unexpected temperatures lying between the CO_2 condensation point and the one of defrosted areas in the cryptic area [*Kieffer et al.*, 2000; *Titus et al.*, 2007]. Investigating different regions exhibiting a cryptic behavior, we have observed that the dark spots were associated with both weaker CO_2 ice signature and higher temperature than the one of CO_2 ice, consistent with the presence of a "thick" layer of dark material on top of the ice.

[76] Observations show that the ejection(s) of dark material occurs in early spring (between Ls 175 and Ls 210), but the surface temperature remains around $T_{\mathrm{cond}}^{\mathrm{surf}}$ prior to Ls 200. Solar insolation during that period is too low to rise the temperature significantly. Modeling also suggests that some CO_2 recondensation on top of the dark material can occur at that period, as the dark material layer acts as a cold trap. After Ls 200, THEMIS temperature data exhibit heterogeneities where the warmest spots correspond to concentrations of dark material. The temperature of these regions increases slowly with time with the darkest areas showing a greater increase, in agreement with modeling results. Unexpectedly, the CO_2 ice signature tends to increase with time after Ls 200 (until the beginning of defrosting), which we interpret to be due to a combination of material movement at different scales and possible CO_2 gas recondensation.

[77] The thermal modeling of dark material-covered CO_2 ice has provided estimations of the thickness of dark material, which range from a few hundreds of microns to a few millimeters in the warmest spots. These estimates however can only apply at the local scale, because of potentially heterogeneous THEMIS pixels.

[78] The nature of the venting process and the amount of material that is moved lead to the conclusion that it could have an impact on the surface properties in the polar regions. Such processes may also occur al lower latitude where slab ice is present. Thus, we suggest that not only polar regions are affected by the vents but also potentially part of the middle- to high-latitudes regions, in particular during periods of high obliquity where CO_2 ice seasonal cap extends toward lower latitudes.

[79] As CO_2 ice dynamics more and more appears to be a key in different active processes on Mars, this survey provides new clues to better understand and quantify its effect on the surface and near subsurface. As its dynamics is strongly influenced by its properties (grain size and impurities), experimental work would be required in the future to better understand CO_2 ice microphysics and its evolution in Martian conditions.

[80] **Acknowledgments.** We would like to thank the THEMIS and CRISM teams for providing the data and helping in the processing. We are also grateful to the JMARS team for making available their software. We thank P. Christensen, M. Vincendon, and S. Douté for fruitful discussions about these exotic polar processes. Finally, we are grateful to the two anonymous reviewers who provided constructive reviews that helped improving the manuscript.

References

Appéré, T., B. Schmitt, Y. Langevin, S. Douté, A. Pommerol, F. Forget, A. Spiga, B. Gondet, and J.-P. Bibring (2011), Winter and spring evolution of northern seasonal deposits on Mars from OMEGA on Mars Express, *J. Geophys. Res.*, *116*, E05001, doi:10.1029/2010JE003762.

Bibring, J., et al. (2004), Perennial water ice identified in the south polar cap of Mars, *Nature*, *428*, 627–630.

Brown, A. J., W. M. Calvin, P. C. McGuire, and S. L. Murchie (2010), Compact Reconnaissance Imaging Spectrometer for Mars (CRISM) south polar mapping: First Mars year of observations, *J. Geophys. Res.*, *115*, E00D13, doi:10.1029/2009JE003333.

Christensen, P. R., et al. (2001), Mars Global Surveyor Thermal Emission Spectrometer experiment: Investigation description and surface science results, *J. Geophys. Res.*, 23,823–23,872.

Christensen, P. R., et al. (2004), The Thermal Emission Imaging System (THEMIS) for the Mars 2001 Odyssey mission, *Space Sci. Rev.*, *110*, 85–130, doi:10.1023/B:SPAC.0000 021008.16305.94.

Colaprete, A., J. R. Barnes, R. M. Haberle, J. L. Hollingsworth, H. H. Kieffer, and T. N. Titus (2005), Albedo of the south pole on Mars determined by topographic forcing of atmosphere dynamics, *Nature*, *435*, 184–188, doi:10.1038/nature03561.

Edwards, C. S., J. L. Bandfield, P. R. Christensen, and R. L. Fergason (2009), Global distribution of bedrock exposures on Mars using THEMIS high-resolution thermal inertia, *J. Geophys. Res.*, *114*, E11001, doi:10.1029/2009JE003363.

Forget, F., F. Hourdin, R. Fournier, C. Hourdin, O. Talagrand, M. Collins, S. R. Lewis, P. L. Read, and J.-P. Huot (1999), Improved general circulation models of the Martian atmosphere from the surface to above 80 km, *J. Geophys. Res.*, *104*, 24,155–24,176.

Hansen, C. J., N. Thomas, G. Portyankina, A. McEwen, T. Becker, S. Byrne, K. Herkenhoff, H. Kieffer, and M. Mellon (2010a), HiRISE observations of gas sublimation-driven activity in Mars southern polar regions: I. Erosion of the surface, *Icarus*, *205*, 283–295, doi:10.1016/j.icarus.2009.07.021.

Hansen, C. J., G. Portyankina, N. Thomas, S. Byrne, and A. McEwen (2010b), HiRISE Images of spring on Mars, paper presented at 41st Lunar and Planetary Science Conference, The Woodlands, Texas.

James, P. B., H. H. Kieffer, and D. A. Paige (1992), The seasonal cycle of carbon dioxide on Mars, in *Mars*, edited by H. H. Kieffer et al., pp. 934–968, Univ. of Ariz. Press, Tucson.

Kieffer, H. H. (2007), Cold jets in the Martian polar caps, *J. Geophys. Res.*, *112*, E08005, doi:10.1029/2006JE002816.

Kieffer, H. H., T. N. Titus, K. F. Mullins, and P. R. Christensen (2000), Mars South polar spring and summer behavior observed by TES: Seasonal cap evolution controlled by frost grain size, *J. Geophys. Res.*, *105*, 9653–9700.

Kieffer, H. H., P. R. Christensen, and T. N. Titus (2006), CO2 jets formed by sublimation beneath translucent slab ice in Mars' seasonal South Polar ice cap, *Nature*, *442*, 793–796, doi:10.1038/nature04945.

Kreslavsky, M. A., J. W. Head, and D. R. Marchant (2008), Periods of active permafrost layer formation during the geological history of Mars: Implications for circum-polar and mid-latitude surface processes, *Planet. Space Sci.*, *56*, 289–302, doi:10.1016/j.pss.2006.02.010.

Langevin, Y., S. Douté, M. Vincendon, F. Poulet, J.-P. Bibring, B. Gondet, B. Schmitt, and F. Forget (2006), No signature of clear CO_2 ice from the 'cryptic' regions in Mars' South Seasonal polar cap, *Nature*, *442*, 790–792, doi:10.1038/nature05012.

Langevin, Y., J.-P. Bibring, F. Montmessin, F. Forget, M. Vincendon, S. Douté, F. Poulet, and B. Gondet (2007), Observations of the south seasonal cap of Mars during recession in 2004–2006 by the OMEGA visible/near-infrared imaging spectrometer on board Mars Express, *J. Geophys. Res.*, *112*, E08S12, doi:10.1029/2006JE002841.

Malin, M. C., and K. S. Edgett (2000), Frosting and defrosting of Martian polar dunes, paper presented at Lunar and Planetary Science Conference XXXI, Houston, TX.

Morgan, F., F. Seelos, S. Murchie, and the CRISM team (2009), CRISM data users' workshop CAT tutorial, paper presented at the MRO/CRISM Data Users' Workshop 2009, John Hopkins Univ. Appl. Phys. Lab., The Woodlands, Tex.

Murchie, S., et al. (2007), Compact Reconnaissance Imaging Spectrometer for Mars (CRISM) on Mars Reconnaissance Orbiter (MRO), *J. Geophys. Res.*, *112*, E05S03, doi:10.1029/2006JE002682.

Paige, D. A., and K. D. Keegan (1994), Thermal and albedo mapping of the polar regions of Mars using Viking thermal mapper observations: 2. South polar region, *J. Geophys. Res.*, *99*, 25,993–26,013, doi:10.1029/93JE03429.

Pilorget, C., F. Forget, E. Millour, M. Vincendon, and J. B. Madeleine (2011), Dark spots and cold jets in the polar regions of Mars: New clues from a thermal model of surface CO_2 ice, *Icarus*, *213*, 131–149, doi:10.1016/j.icarus.2011.01.031.

Piqueux, S., and P. R. Christensen (2008), North and south subice gas flow and venting of the seasonal caps of Mars: A major geomorphological agent, *J. Geophys. Res.*, *113*, E06005, doi:10.1029/2007JE003009.

Piqueux, S., and P. R. Christensen (2011), Temperature-dependent thermal inertia of homogeneous Martian regolith, *J. Geophys. Res.*, *116*, E07004, doi:10.1029/2011JE003805.

Piqueux, S., S. Byrne, and M. I. Richardson (2003), Sublimation of Mars's Southern seasonal CO2 ice cap and the formation of spiders, *J. Geophys. Res.*, *108*, 5084, doi:10.1029/2002JE002007.

Pommerol, A., G. Portyankina, N. Thomas, K.-M. Aye, C. J. Hansen, M. Vincendon, and Y. Langevin (2011), Evolution of south seasonal cap during Martian spring: Insights from high-resolution observations by HiRISE and CRISM on Mars Reconnaissance Orbiter, *J. Geophys. Res.*, *116*, E08007, doi:10.1029/2010JE003790.

Portyankina, G., W. J. Markiewicz, N. Thomas, C. J. Hansen, and M. Milazzo (2010), HiRISE observations of gas sublimation-driven activity in Mars southern polar regions: III. Models of processes involving translucent ice, *Icarus*, *205*, 311–320, doi:10.1016/j.icarus.2009.08.029.

Smith, M. D., J. L. Bandfield, and P. R. Christensen (2000a), Separation of atmospheric and surface spectral features in Mars Global Surveyor Thermal Emission Spectrometer (TES) spectra, *J. Geophys. Res.*, *105*, 9589–9608, doi:10.1029/1999JE001105.

Smith, M. D., J. C. Pearl, B. J. Conrath, and P. R. Christensen (2000b), Mars Global Surveyor Thermal Emission Spectrometer (TES) observations of dust opacity during aerobraking and science phasing, *J. Geophys. Res.*, *105*, 9539–9552, doi:10.1029/1999JE001097.

Supulver, K. D., K. S. Edgett, and M. C. Malin (2001), Seasonal Changes in frost cover in the Martian South Polar Region: Mars Global Surveyor MOC and TES Monitoring of the Richardson Crater Dune Field, 32nd Annual Lunar and Planetary Science Conference, Houston, Texas.

Thomas, N., C. J. Hansen, G. Portyankina, and P. S. Russell (2010), HiRISE observations of gas sublimation-driven activity in Mars southern polar regions: II. Surficial deposits and their origins, *Icarus*, *205*, 296–310, doi:10.1016/j.icarus.2009.05.030.

Titus, T. N., H. H. Kieffer, K. F. Mullins, and P. R. Christensen (2001), TES premapping data: Slab ice and snow flurries in the Martian north polar night, *J. Geophys. Res.*, *106*, 23,181–23,196.

Titus, T. N., Y. Langevin, S. L. Murchie, F. Seelos, H. H. Kieffer, and Crism Scienceteam (2007), MRO CRISM observations of the South Polar Cryptic Region, Seventh International Conference on Mars, Pasadena, California.

Titus, T. N., H. H. Kieffer, Y. Langevin, S. Murchie, F. Seelos, and M. Vincendon (2007b), Bright fans in Mars cryptic region caused by adiabatic cooling of CO2 gas jets, Abstract #P24A-05 presented at 2007 Fall Meeting, AGU, San Franciso, Calif.

Vincendon, M., and Y. Langevin (2010), A spherical Monte-Carlo model of aerosols: Validation and first applications to Mars and Titan, *Icarus*, *207*, 923–931, doi:10.1016/j.icarus.2009.12.018.

Warren, S. G., W. J. Wiscombe, and J. F. Firestone (1990), Spectral albedo and emissivity of CO_2 in Martian polar caps: Model results, *J. Geophys. Res.*, *95*, 717–741.